Development of Sn–Ag–Cu and Sn–Ag–Cu–X alloys for Pb-free electronic solder applications

Iver E. Anderson

Published online: 27 September 2006

Abstract The global electronic assembly community is striving to accommodate the replacement of Pb-containing solders, primarily Sn–Pb alloys, with Pb-free solders due to environmental regulations and market pressures. Of the Pb-free choices, a family of solder alloys based on the Sn–Ag–Cu (SAC) ternary eutectic ($T_{eut.}$ = 217°C) composition have emerged with the most potential for broad use across the industry, but the preferred (typically near-eutectic) composition is still in debate. This review will attempt to clarify the characteristic microstructures and mechanical properties of the current candidates and recommend alloy choices, a maximum operating temperature limit, and directions for future work. Also included in this review will be an exploration of several SAC + X candidates, i.e., 4th element modifications of SAC solder alloys, that are intended to control solder alloy undercooling and solidification product phases and to improve the resistance of SAC solder joints to high temperature thermal aging effects. Again, preliminary alloy recommendations will be offered, along with suggestions for future work.

1 Introduction

The replacement of Sn–Pb solders for assembly of electronic systems is being driven by impending environmental regulations [1–3] and global market pressures to utilize Pb-free solders. During this major transition involving substitution for a near-universal joining material system, eutectic or near-eutectic Sn–Pb solder, there is also the opportunity to make a major improvement in joint reliability for challenging operating environments, i.e., high temperatures and stress levels, as well as impact loading situations. To help realize this opportunity, investigations into a promising alloy ''family'' of eutectic and near-eutectic Sn–Ag–Cu (SAC) solders [4, 5] have increased at many different laboratories, worldwide [6–9]. Since the Sn–Ag–Cu ternary eutectic temperature of 217°C is significantly higher than 183°C for Sn–37Pb (wt.%), it should be said that Pb-free SAC solder is not a ''drop-in'' replacement for Sn–Pb in the highly refined electronics assembly sequence, e.g., for surface mount technology (SMT) [2, 9]. While the enhanced reflow temperatures of 235–255°C for SAC near-eutectic solder, compared to approximately 220°C for Sn–Pb eutectic, are within the capabilities of current reflow ovens, some of the component packages and circuit board materials, primarily polymeric, need to be upgraded to withstand these higher processing temperatures. In addition, the transition must be made to an alternative Pb-free component lead coating to replace Sn–Pb. Also, a Pb-free high/low temperature solder hierarchy pair, to replace Sn–95Pb/Sn–37Pb, needs to be developed that includes (presumably) SAC solder and another Pb-free alloy to permit effective multi-chip module assembly [2, 9]. In spite of these complications, the electronics industry has seized the challenge and is proceeding forward rapidly to develop the assembly techniques and to generate the reliability data for Sn–Ag–Cu as a preferred Pb-free solder in many electronic assembly applications [2, 9].

I. E. Anderson (✉)
Ames Laboratory (USDOE), Iowa State University,
222 Metals Development Building, Ames, IA 50011, USA
e-mail: andersoni@ameslab.gov

Compared to Sn–Pb solders that have been limited typically to low stress joints and reduced temperature service because of the soft Pb phase that is prone to coarsening and ductile creep failure [10], the high Sn content and strong intermetallic phases of a well designed Sn–Ag–Cu alloy solder can promote enhanced joint strength and creep resistance [11], and can permit an increased operating temperature envelope for advanced electronic systems and devices. Results of SAC alloy development have demonstrated increased shear strength at ambient and elevated temperatures, e.g., 150°C, resistance to isothermal fatigue [12], and resistance to thermal aging during temperature excursions up to about 150°C, the current test standards for under-the-hood automotive electronics [13]. In terms of mechanical properties, shear strength [14], rather than joint tensile strength, will be the focus of the property characterization results that are included in this review due to the importance of shear failures in electronic systems with mismatched coefficients of thermal expansion [2, 15]. Also, early tensile failure studies showed that essentially all solder joints with Sn-based solders would exhibit the same type of localized parting at fairly low stress of the solder matrix and the Cu_6Sn_5 intermetallic layer, with little possibility of discriminating between solder alloy effects [10]. Although important for reliability testing of specific electronic assembly applications [16], thermal–mechanical fatigue analysis results also will not be included in this review since many of the novel SAC alloying concepts, with some exceptions [16], have not been tested for TMF, but typically have been tested in shear. In the expanding world of portable electronics and miniaturization of electronic devices, the ability of circuitry to remain undamaged after a drop impact [9, 17–21] is becoming another key objective for SAC solder joint microstructure design. Modified Izod impact test results will be reviewed because such impact testing is simple to practice and very useful for quantitative ranking in alloy design and thermal aging studies [17, 18], compared to board level drop testing [20].

Superior levels of these solder joint mechanical properties can be accomplished by microstructural control approaches, starting with the as-solidified solder joint [8, 22–28], i.e., tailoring of the as-solidified intermetallic interface with the substrate and controlling of solidification nucleation for the solder matrix. While substrate/solder interface tailoring is practiced by alloy additions to the SAC solder or metallization (coating) of the substrate, the issue of nucleation control for the solder matrix has been addressed by both SAC alloy variations and by fourth element additions. It should be noted that the solidification microstructures of Sn–Pb eutectic and near-eutectic solders are not nearly as sensitive to cooling rate and composition variations as the near-eutectic Sn–Ag–Cu solders [9]. This sensitivity is due primarily to the characteristic of Sn and Sn-enriched alloys for high undercooling prior to solidification [9]. It should be noted that a significant portion of the fundamental research on microstructural control of SAC solder joints has been done for the general case of bonding to Cu conductors and this review will be limited to the Cu substrate case. The common industrial case of solder bonding to one of several types of multi-layer metallization surfaces and the consequences of multiple reflow cycles has also been studied in detail, but has been covered in other reviews [29–34].

Another focus of this review will be on microstructural control for the thermally aged solder matrix/intermetallic interface region of SAC solder joints, in particular. Motivation for these recent studies was provided [20, 35, 36] by reported problems with pore development/coalescence and brittle fracture along the intermetallic (Cu_3Sn) interface with a Cu substrate. Recent studies [9, 35, 36] on accelerated aging of SAC alloy joints report that the suppression of voids, and especially suppression of void coalescence, in the intermetallic interfacial region is promoted by fourth element additions, eliminating an apparent embrittlement precursor in coarsened SAC solder joints. Interestingly, some of the same fourth element additions have been useful for both nucleation control and for resistance to aging effects.

2 Ternary Pb-free solder joint microstructures and mechanical properties

A closely related set of Sn–Ag–Cu near-eutectic alloys have risen through the ranks of many experimental studies to stand as the most likely candidates for widespread replacement of Sn–Pb solders [9, 26, 37]. As an improvement over the previous Sn–Ag eutectic solder in Pb-free electronic assembly applications, the Sn–Ag–Cu solders offer a reduced melting temperature (about 4°C lower) and additional tolerance for variations in cooling rate after reflow [9, 26, 37]. Prior calorimetric studies [26] revealed the very similar melting behavior of several closely related Sn–Ag–Cu alloys, consistent with the phase diagram studies [6] on this system. Compared to other common choices, the Cu alloy addition to Sn–Ag is abundant and low cost, e.g., lower cost than In, is an aid to wetting and does not increase drossing, unlike Zn [29], is compatible

with common no-clean paste fluxes [38], and is not a by-product of Pb mining, e.g., unlike Bi and Sb [29].

As an indication of the Sn–3.5Ag (wt.%) baseline solder alloy joint characteristics, Fig. 1a shows a low magnification optical micrograph of an etched cross-section [39]. Sn dendrites appear to extend directly across the full 70 μm width of this joint with a secondary dendrite arm spacing (SDAS) of about 5 μm. Optical microscopy seems to be better suited than SEM for revealing a long range dendritic solidification morphology in these joints, clarifying the distinctions between cells and dendrites [39]. The typical Cu_6Sn_5 intermetallic phase at the interface of the Cu substrate and the solder matrix exhibits some faceting and a thickness of approximately 2 μm, as revealed in Fig. 1b, consistent with previous results [26].

2.1 Solidification microstructures and shear strength for near-eutectic SAC solders

In comparison to Sn–Pb solders, a successful Sn–Ag–Cu alloy solder should exhibit enhanced shear strength at ambient temperature. Perhaps more importantly, the Sn–Ag–Cu solder should display improved creep strength and resistance to thermal–mechanical fatigue during temperature excursions up to about, e.g., 150°C, the current maximum operating temperature limit of under-the-hood automotive electronics [13]. This can be accomplished by microstructural strengthening approaches for the solder matrix. Essentially, the matrix strengthening strategy is to avoid or refine Sn dendrites, to minimize or refine any pro-eutectic intermetallic phases, and to increase the fraction of fine eutectic in the as-solidified joint [40]. To implement the matrix strengthening approach, four Sn–Ag–Cu solder alloys were selected for a previous study [39] which fall in a composition region that includes and closely surrounds the calculated ternary eutectic composition [6] of Sn–3.7Ag–0.9Cu (wt.%), as shown in Fig. 2. Two alloy choices, Sn–3.0Ag–0.5Cu (outlined by a triangle in Fig. 2) and Sn–3.9Ag–0.6Cu (outlined by a circle in Fig. 2), were chosen to correspond to alloys being studied actively by JEIDA and NEMI [37], respectively. Another alloy, Sn–3.6Ag–1.0Cu (outlined by a hexagon in Fig. 2), was included to provide a correspondence to other previous studies [26]. The melting behavior of three of the four alloys (excluding Sn–3.9Ag–0.6Cu) was also studied by differential thermal analysis [26] and was determined to be closely related, with a clear eutectic melting onset at 217°C and a slightly extended liquidus melting signal, consistent with near-eutectic alloys.

It should be noted that the solidification microstructures of other ternary Sn–Ag–Cu alloys certainly have been studied and some of these will be cited in this review. However, this set of solder alloy joints were prepared under identical conditions and were intended as a representative survey of the different relevant regions of the ternary phase diagram that are likely to be used for solder applications. Although a hand soldering technique [39] was used, the temperature ramp, peak temperature (255°C), cooling conditions (1–3°C/s), and Cu substrates were intended to simulate typical reflow parameters for common circuit assembly practice, to provide a comparison of the microstructure results with practical technological value.

The optical micrographs [39] of Fig. 3 show the significant effects on the as-solidified joint microstructures of fairly minor variations in Ag and Cu content in the near-eutectic Sn–Ag–Cu solder alloys used to make the joints. The rather coarse Sn dendrites for Sn–3.0Ag–0.5Cu in Fig. 3a, with a secondary dendrite arm spacing (SDAS) of about 6–10 μm, can be compared to the extremely fine Sn dendrites for Sn–3.9Ag–0.6Cu in Fig. 3b, with an SDAS of about 2 μm. Also, the Sn dendrite pattern associated with Sn–3.7Ag–0.9Cu in Fig. 3c has a very similar spacing to the Sn dendrites of Fig. 2a, associated with Sn–3.5Ag. In contrast, the

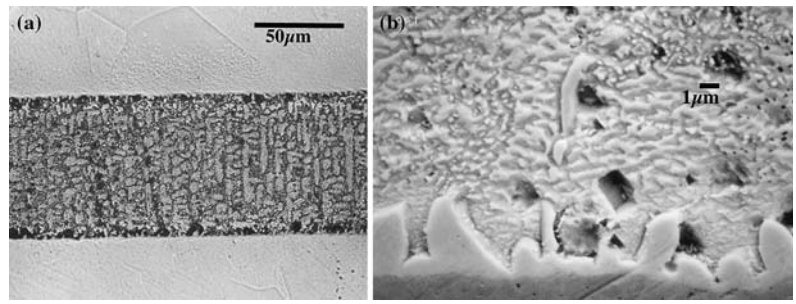

Fig. 1 Cross-section microstructure of as-solidified solder joints made from Sn–3.5Ag (wt.%), including, (**a**) optical micrograph of joint with Cu substrate on top and bottom, (**b**) SEM micrograph (backscattered electron imaging-BEI) with Cu substrate on bottom [39]

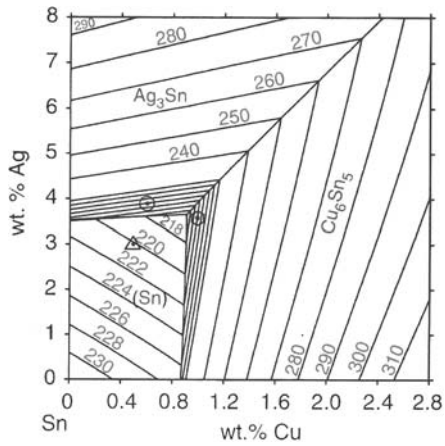

Fig. 2 The composition region that closely surrounds the calculated ternary eutectic composition of Sn–3.7Ag–0.9Cu (wt.%), as seen from the calculated liquidus surface [6, 39]

solidification morphology associated with Sn–3.6Ag–1.0Cu in Fig. 3d does not appear dendritic, certainly not with any extended Sn dendrites. Moreover, the large Ag_3Sn ''needle'' phases in Fig. 3b, as confirmed by energy dispersive spectroscopy (EDS) in the SEM, that project from the upper intermetallic layer into the solder matrix, distinguished this Sn–3.9Ag–0.6Cu microstructure from the others in Fig. 3.

The higher magnification and atomic number contrast of the SEM-BEI micrographs [39] in Fig. 4 provide additional information on the as-solidified joint microstructures shown in Fig. 3. For example, from Fig. 4d it seems that, rather than Sn, Cu_6Sn_5 is the apparent primary (pro-eutectic) phase in the solidification of Sn–3.6Ag–1.0Cu solder, as confirmed by EDS in the SEM, followed by solidification of an extremely fine ternary eutectic. Also, the coarser Sn dendrite patterns of Fig. 4a (Sn–3.0Ag–0.5Cu) and Fig. 4c (Sn–3.7Ag–0.9Cu) allow for wider regions of ternary eutectic, compared to Fig. 4b (Sn–3.9Ag–0.6Cu). An interesting difference in the intermetallic at the Cu/solder interface is also apparent, where the partially faceted Cu_6Sn_5 fingers of Fig. 4b (Sn–3.9Ag–0.6Cu) and 4c (Sn–3.7Ag–0.9Cu) contrast with the finely spaced rounded stubs of Fig. 4d (Sn–3.6Ag–1.0Cu) and the widely spaced projections of Fig. 4a (Sn–3.0Ag–0.5Cu).

Although the ternary eutectic alloy, Sn–3.7Ag–0.9Cu, calculated from experimental and thermodynamic data [6] would be expected to have an equilibrium structure that consists of mixture of three phases: β-Sn, Ag_3Sn, and Cu_6Sn_5, with volume fractions consistent with the phase diagram [6], the actual joint microstructure in Figs. 3c and 4c is more complex. It appears that the joint made from Sn–3.7Ag–0.9Cu exhibits Sn primary dendrites with a fine uniform ternary eutectic structure in the interdendritic regions. If the calculated ternary eutectic composition is correct, the appearance of primary Sn dendrites in this alloy is evidence for some significant undercooling of the solder joint [6], where the Sn phase probably solidified at a temperature beneath the coupled eutectic growth region [41]. Some studies on undercooling of bulk samples of similar solder alloys, along with pure Sn and Pb, demonstrated that a Sn–3.8Ag–0.7Cu near-eutectic alloy can under-

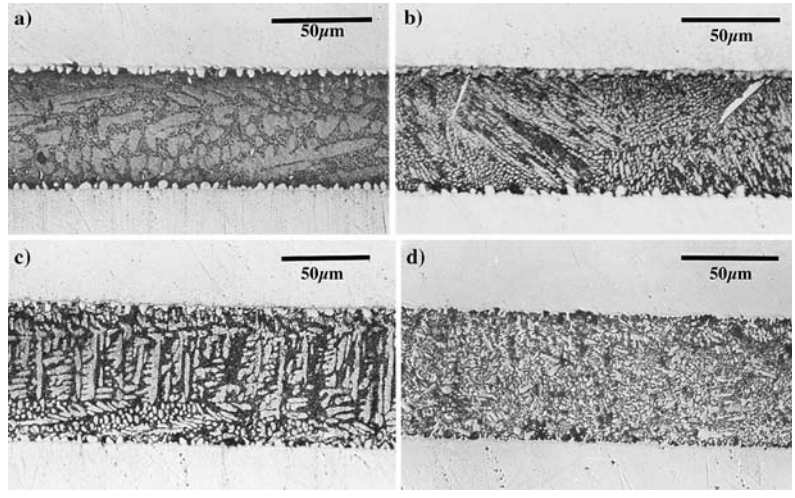

Fig. 3 Optical micrographs of as-solidified solder joints made from (**a**) Sn–3.0Ag–0.5Cu, (**b**) Sn–3.9Ag–0.6Cu, (**c**) Sn–3.7Ag–0.9Cu, and (**d**) Sn–3.6Ag–1.0Cu [39]

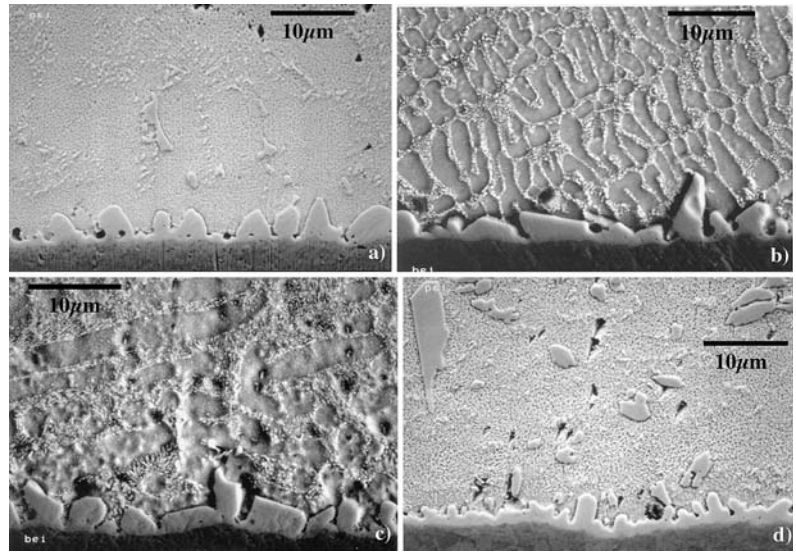

Fig. 4 SEM micrographs (BEI) of as-solidified solder joints made from (**a**) Sn–3.0Ag–0.5Cu, (**b**) Sn–3.9Ag–0.6Cu, (**c**) Sn–3.7Ag–0.9Cu, and (**d**) Sn–3.6Ag–1.0Cu [39]

cool nearly 30°C before nucleation of solidification and other similar SAC alloys had undercoolings from 18°C to 35°C [42]. Moreover in the Sn–Ag–Cu (SAC) alloy system, both intermetallic phases in the eutectic, Ag_3Sn and Cu_6Sn_5, are known to be faceted [41], which would be expected to skew the coupled eutectic growth region, promoting primary Sn phase nucleation and growth for a eutectic alloy even at modest undercoolings [6].

The tendency for high undercooling and Sn dendrite formation of the ternary eutectic SAC alloy can be contrasted with the observed solidification behavior for the Sn–Pb solders, which do not undercool appreciably, only 3–4°C, and exhibit a fairly uniform coupled (irregular) eutectic structure over a wide range of cooling rates [9]. Generally, in Sn–Pb alloys an increased cooling rate during solidification results in a refined eutectic microstructure with enhanced strength, in a continuous trend. For eutectic and most near-eutectic SAC solder alloys, instead of coupled eutectic solidification, melt undercooling and the nucleation and growth of Sn dendrites is a less controlled phenomenon. However, it is generally true that rapid cooling of SAC alloys (>5–10°C/s) typically will result in a highly refined microstructure with fine dendrites and interdendritic ternary eutectic that has significantly enhanced strength [9]. On the other hand, slow cooling of SAC alloys (< 1–3°C/s) will result in Sn dendrites, probably with a larger dendrite arm spacing, and interdendritic eutectic, but formation of massive pro-eutectic intermetallic phases may precede Sn nucleation, as will be discussed below. Thus, slow-cooled SAC solder joints may be more ductile or more brittle, depending on whether massive intermetallic phases are able to nucleate and grow.

To illustrate the composition dependence of these SAC solidification characteristics, three near-eutectic SAC alloy were used to make solder joints that were all cooled at the same rate, 1–3°C/s from the same reflow peak temperature, 255°C. Melt undercooling and Sn dendrite nucleation and growth appear to have affected the solidification of two of the three near-eutectic alloys shown above, Sn–3.0Ag–0.5Cu and Sn–3.9Ag–0.6Cu in different ways, but not to the extent that it changed the equilibrium primary (pro-eutectic) phases expected from the calculated phase diagram in Fig. 2 [39]. In other words, the Sn dendrites in Fig. 3a are the predicted primary phase in Sn–3.0Ag–0.5Cu and the coarse dendrite arm spacing implies that they grew at a reduced velocity, consistent with a reduced undercooling [39]. In addition, the Ag_3Sn primary phase plates in Fig. 3b also are the predicted primary (pro-eutectic) phase for Sn–3.9Ag–0.6Cu, but the very fine Sn dendrites in the majority of the solder matrix are consistent with rapid growth from a highly undercooled melt. Although the undercooling could not be estimated qualitatively from the microstructure for the Sn–3.6Ag–1.0Cu alloy in Figs. 3d and 4d, the lack of Sn dendrites and the formation of primary (pro-eutectic) Cu_6Sn_5 phase particles, apparently randomly dispersed

in a ternary eutectic matrix, is expected from the phase diagram [39].

Based on this representative set of microstructure observations, it is useful to compare the criteria described above for ideal microstructural strengthening of the solder matrix to the results for the as-solidified solder joints. To restate, the matrix strengthening strategy is to avoid or refine Sn dendrites, to avoid or refine any pro-eutectic intermetallic phases, and to increase the fraction of fine eutectic in the as-solidified joint. Of the four choices above, including the calculated eutectic composition, Sn–3.7Ag–0.9Cu, the most promising appears to be Sn–3.6Ag–1.0Cu which has a joint microstructure that is dominated by a highly refined ternary eutectic and is decorated by small (10 μm or less) pro-eutectic Cu_6Sn_5 phase regions. In terms of microstructural strengthening, this type of as-solidified microstructure would be expected to have an enhanced shear strength that is dominated by the fine eutectic and would tend to deform uniformly if stressed beyond the yield point. In contrast, a joint formed from Sn–3.0Ag–0.5Cu solder with coarse Sn dendrites and interdendritic ternary eutectic would be expected to have a reduced shear strength that is dominated by the low yield point of the nearly pure Sn phase and would deform in a ductile manner within the dendritic regions.

A summary [39] of the ambient temperature shear strength results for all of the alloys that are illustrated above are shown in Fig. 5, along with the results from two modified SAC alloys containing either Co or Fe additions that will be discussed below. An indication of the repeatability of the maximum shear strength values is given by the narrow range (± 2.5–5 MPa) of the standard deviation of the measurements, where at least seven specimens were tested for each type of solder joint. The weakest of the solder joints was made from the Sn–3.0Ag–0.5Cu, while the strongest SAC solder joints were made from Sn–3.6Ag–1.0Cu, consistent with the predictions of the microstructural analysis from above. The shear strength of the baseline Sn–3.5Ag solder joints fell in the middle of the range of values. This apparent strengthening may be due to the sensitivity of the Sn–3.5Ag solder microstructure to reflow and solidification conditions and the Cu dissolution phenomenon, as discussed below [26, 43–45]. The difference between the maximum shear strength and the apparent yield strength is an indication of the reasonable ductility exhibited by these samples, although the yield strength values had an increased standard deviation. It is also interesting to note that the joints made with Sn–3.6Ag–1.0Cu also exhibited the highest yield strength with the lowest scatter of the data, suggesting a very consistent microstructure.

In addition to selection of a SAC solder alloy based on as-solidified joint strength, where increased strength is preferred within reasonable limits [16], another criteria should be the type of joint failure mechanism, where uniform yielding and ductile failure are preferred. It is important to note that the solidification of relatively large plates of Ag_3Sn in a Sn–Ag–Cu solder microstructure was shown to be particularly detrimental to the fracture behavior and thermal-fatigue life of solder joints, promoting brittle failure along interfaces between Ag_3Sn and β-Sn at reduced stress and shorter joint life [42]. Motivated by these observations, an extensive effort has been devoted to improved SAC solder alloy design to eliminate the occurrence of Ag_3Sn pro-eutectic nucleation [9, 42], leading to a patent [46]. This effort quantified the

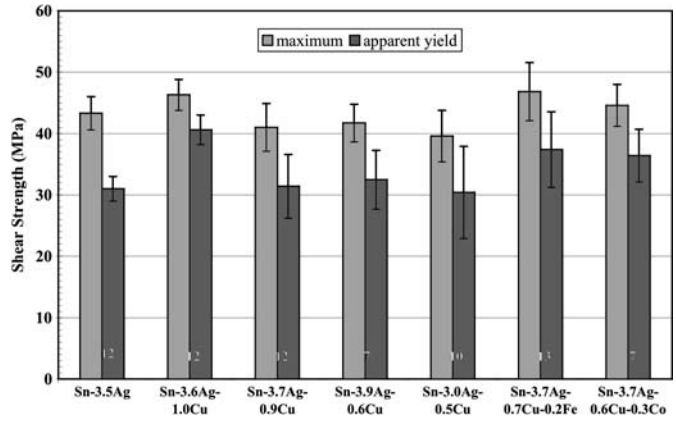

Fig. 5 Summary of asymmetric four point bend (AFPB) shear strength tests at ambient temperature on as-solidified solder joints made from the alloys listed along the *x*-axis. The number of repeat samples for each alloy is indicated in light contrast on each set, along with the standard deviation of the values at the top of each bar [39]

effect of independent variations of Ag and Cu content on the formation of Ag_3Sn and used 3.8Ag and 0.9Cu as maximum levels of each element [42]. In one part of the study, the composition dependent solidification of independent solder alloy balls was characterized and the same solder balls were also solidified between Cu substrates to form joints. From the results, some general recommendations were to utilize a Ag content of 2.0–3.0 wt.% and a Cu content of about 0.7 wt.%, which would suppress Ag_3Sn formation and still maintain a pasty range (difference between liquidus and solidus temperatures) less than 3.5°C, i.e., near-eutectic behavior [42]. For example, one SAC alloy mentioned specifically was Sn–2.7Ag–0.7Cu as representing an upper limit (for Ag content) for possible formation of Ag_3Sn plates, even at extremely slow-cooled conditions (0.02°C/s) [42]. From the position of this alloy on the liquidus surface of the calculated phase diagram (see Fig. 2), the solidified microstructure of a joint prepared from Sn–2.7Ag–0.7Cu in the same manner as the ones shown in Figs. 2–4 should be similar to Figs. 3a and 4a that were made from Sn–3.0Ag–0.5Cu.

2.2 Preliminary recommendation for SAC solders

Thus, to avoid the formation of Ag_3Sn plates according to the findings of the previous extensive study [9, 42], one must choose a solder joint of reduced strength, perhaps Sn–2.7Ag–0.7Cu. Alternatively, to avoid nucleation of massive Ag_3Sn plates and to maintain enhanced solder joint strength, a SAC composition of Sn–3.6Ag–1.0Cu could be picked [39], which exhibits pro-eutectic nucleation of a well distributed Cu_6Sn_5 phase, followed by ternary eutectic solidification, effectively precluding nucleation of massive Ag_3Sn plates and long range Sn dendrites. However, it is recommended that future work with this type of SAC alloy should focus on a small composition region with slightly lower Ag and Cu, perhaps Sn–3.5Ag–0.95Cu. The advantage could be a similar joint solidification path, a reduced amount of pro-eutectic Cu_6Sn_5, and a significantly smaller pasty range. According to the calculated liquidus surface in Fig. 2, Sn–3.6Ag–1.0Cu has a pasty range of about 5°C, compared to about 3°C for Sn–3.5Ag–0.95Cu, assuming a solidus temperature that is equivalent to the ternary eutectic of 217°C. If this apparent mechanism is used properly, it should be possible to generate a very high fraction of ternary eutectic structure from a very slightly off-eutectic composition by accepting the inclusion of a small fraction of well-distributed Cu_6Sn_5 pro-eutectic phase.

It should be noted also that the effect of Cu dissolution from the substrates on the solder matrix alloy composition is not included in this discussion. Thus, the possible precision for adjustment of Cu content in some SAC alloy solders is open to question, i.e., precise control of the final joint composition. A previous estimate of the Cu dissolution effect was an increase of roughly 0.5% Cu to the solder joint above the initial alloy composition, depending on the reflow conditions [47]. Some recent studies that involve the Cu pick-up phenomenon in Sn-enriched solder alloys have been reported [36, 45], but the difficulty of probing this effect is well recognized, especially by micro-analytical techniques [48]. One data point for Cu solubility in Sn is the maximum level (2.2 wt.%) that can be retained by rapid quenching, followed by cryogenic X-ray diffraction of the structure [49]. Vianco reported [36] that a maximum local concentration enhancement of about 2% was measured by a wavelength dispersive spectroscopy (WDS) line scan method with an electron microprobe using a highly focused beam method, after soldering of Cu substrates with Sn–3.9Ag–0.6Cu by reflowing at a peak temperature of 260°C. This local maximum Cu content was reported to decrease continuously from the inner edge of the typical Cu_6Sn_5 interfacial layer toward the center of the joint, proceeding from about 2% to a baseline (nominal) value of about 0.6% over a distance of about 10 μm [36]. Also, the existence of interior Cu_6Sn_5 phases (within the joint matrix) was also detected in the Cu and Sn line scans, as peaks and valleys, respectively, by Vianco [36] and others [35, 40]. In a microstructural sense, to measure the true pick-up of Cu into the joint matrix region one must include excess Cu dissolved in Sn and the interior content of Cu_6Sn_5, both as independent phases and as part of the ternary eutectic structure. A broad beam WDS method, most common in analysis of geological specimens [50, 51], has recently been applied to this difficult problem [45]. One encouraging result from this study is that, although low Cu content SAC alloys, e.g., Sn–3.0Ag–0.5Cu, may pick up 0.5–0.7Cu, a solder joint made with Sn–3.7Ag–0.9Cu did not have any significant change in Cu content [45]. Thus, the prospect of closely controlling the final composition (Cu content) of a joint made with Sn–3.5Ag–0.95Cu appears more likely than that of a joint made with a SAC alloy containing only 0.5–0.6Cu.

2.3 Thermally aged microstructures and shear strength for near-eutectic SAC solders

The demand for some electronic assemblies to remain reliable for extremely long times in harsh environments, particularly at high temperatures, is an accelerating trend, e.g., the desired positioning of automotive control systems immediately adjacent to the internal combustion engines that they control [16]. In other words, in these situations it is highly desirable for a Pb-free solder to exhibit increased strength and sufficient ductility, compared to Sn–Pb eutectic solder, at temperatures in the neighborhood of 150°C, as mentioned above [13, 16]. To provide a preliminary test of high temperature performance of a partial set of the SAC solder joints that are included in the discussion above, shear testing of such solder joint samples was conducted at 150°C [39]. A comparison of the maximum shear strength values at ambient temperature to the shear strength values at 150°C is shown in Fig. 6. The results of this elevated temperature test indicated a drop of at least half of the shear strength of the ambient temperature measurements to a range between about 15 MPa and 20 MPa [39]. Due to the increased standard deviation of the measurements, no significant differences can be observed between the elevated temperature shear strengths of the solder joints made from any of the alloys tested. Actually, the collapse of all of the 150°C shear strength values to a single range of 15–20 MPa suggests that the high temperature mechanical properties probably are controlled by the decreased strength of the Sn phase in the solder matrix [39], related to Sn grain growth and Sn inter-granular de-cohesion [52]. Any more detailed analysis of these results is hindered by the dynamic nature of microstructural coarsening that must have occurred during these high temperature tests. Thus, it was decided to conduct future shear strength tests at ambient temperature after fixed periods of high temperature aging and to correlate these results to observations of the aged solder joint microstructures.

As mentioned above, ambient temperature shear strength provided a mechanical property test for ranking of solder joints at two different stages of accelerated (isothermal) aging at 150°C (approximately 0.86 T_m). A summary of the ambient temperature shear test results for the 100 h and 1,000 h aged solder joints of all seven alloys that were shown in Fig. 7, compared to the as-soldered shear strength [35, 53]. In both the as-soldered and 100 h aged conditions, the three weakest solder joints were made from Sn–3.9Ag–0.6Cu, Sn–3.7Ag–0.9Cu, and Sn–3.0Ag–0.5Cu, while the three strongest aged joints were made from Sn–3.7Ag–0.6Cu–0.3Co, Sn–3.6Ag–1.0Cu, and Sn–3.7Ag–0.7Cu–0.2Fe, with the joints made from Sn–3.5Ag in the mid-range of shear strength [35, 53]. After 1,000 h of aging the weakest group still retained the same ranking, but one of the strong alloys, Sn–3.7Ag–0.6Cu–0.3Co, moved to the mid-range and the Sn–3.5Ag results moved into the strong group. If all of the alloy results in Fig. 7 are averaged, the maximum shear strength of these Pb-free solder joints dropped about 20% from the as-soldered condition to the 100 h aged condition, and dropped only another 16% from the 100 h aged condition to the 1,000 h aged condition [35]. Thus, after 1,000 h of aging at 150°C, the average maximum shear strength of the solder joints made from all the alloys in this study retained about two thirds of the as-soldered maximum shear strength. In contrast to the previous 150°C shear testing [39], careful control of the thermally aged microstructures of these joint samples and the use of shear testing at

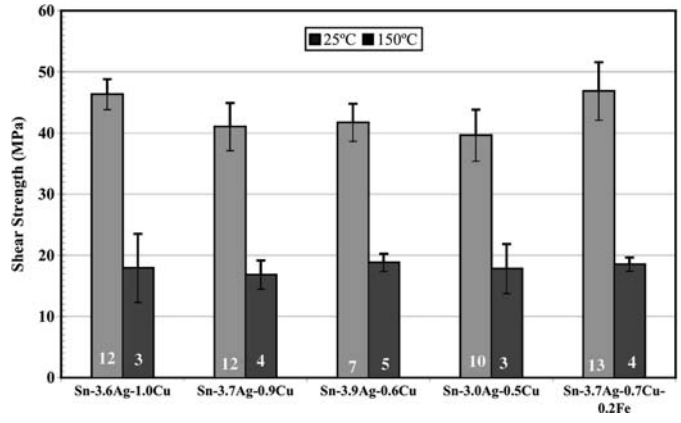

Fig. 6 Summary of asymmetric four point bend tests at ambient and elevated (150°C) temperature on solder joints made from the alloys listed along the *x*-axis. The number of repeat samples for each alloy is indicated in light contrast on each bar, along with the standard deviation of the values at the top of each bar [39]

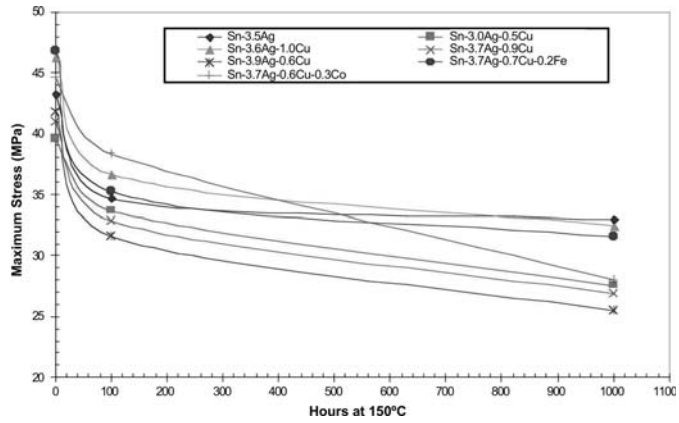

Fig. 7 Summary of maximum shear strength from AFPB tests at ambient temperature on as-soldered and aged solder joints made from the indicated alloys [35, 53]

room temperature provided an improved opportunity [35] to explore any measurable differences between this fairly representative set of SAC solder alloys, given the distinctions already noted in their as-solidified microstructures and properties [39, 53].

To more fully understand the results for maximum shear strength after aging, the load versus elongation data was analyzed and correlated with the corresponding solder joint microstructures and macroscopic joint failure characteristics [35]. Further distinctions between the joint sample microstructures were derived from analysis in both the as-aged and post-shear test conditions [35]. The strongest solder joints after 100 h aging, e.g., made from Sn–3.6Ag–1.0Cu, exhibited considerable ductility and plastic yielding before the maximum shear strength level and considerable plastic yielding after the maximum shear strength was reached (see Fig. 8a). The companion post-shear microstructure in Fig. 8b shows that a significant amount of homogeneous plastic flow had occurred in the solder matrix, suggested by the apparent bending and alignment of the elongated intermetallic phases with the plastic flow direction of the solder matrix [35].

On the other hand, the localized ductile shear behavior of the ''weak'' class of joint samples, represented by the results for Sn–3.7Ag–0.9Cu in Fig. 7, was typical of the less uniform ductile failure mechanism displayed by many of the 100 h aged specimens, both weak and strong [35]. The load versus shear elongation data in Fig. 9a, shows only a small amount of elastic deformation before plastic yielding at about 22 MPa and maximum shear strength at about 32 MPa. As reported by several investigators of shear failures in aged and as-solidified SAC solder joints [11, 54, 55], this non-uniform ductile shear displacement of the solder joint matrix appears to be localized to a portion of the continuous Sn phase that is immediately adjacent to the Cu_6Sn_5 intermetallic interface (see Fig. 9b). There also appears to be some minor amount of intermetallic cracking across projections of the Cu_6Sn_5 and along the interfaces between the Cu_6Sn_5 and the Cu_3Sn layer, which is well known to form during initial aging at such high temperatures [36]. Thus, the failure of both strong and weak solder joints does not seem to involve fracturing of the Cu_3Sn layer, although linking of voids during crack propagation may contribute to weakening of the Cu_6Sn_5/Cu_3Sn interface [35].

In the initial analysis of solder joints after 1,000 h of aging at 150°C there was noted an additional loss of shear strength, averaged for all of the solder alloys studied, of approximately 16% beyond the initial drop after 100 h, as given in Fig. 7. Over the range of alloys studied and within the uncertainty of the intermetallic compound (IMC) layer measurement, neither the thickness of the Cu_3Sn layer nor the total thickness of both intermetallic layers, $Cu_3Sn + Cu_6Sn_5$, had any apparent relationship to the ranking of maximum shear strength after 1,000 h of aging [35], as reported in some studies [36]. However, in contrast to the as-solidified and 100 h aged results, two different types of mechanical deformation behavior were observed for each alloy in the 1,000 h aged results (e.g., Fig. 10a) in most cases, leading to a greater standard deviation of the strength data [35]. The strong joint exhibited almost the same maximum shear strength, ductility, and plastic yielding behavior as the 100 h aged sample in Fig. 8a. Also, the post-shear microstructure in Fig. 10b and c revealed that a significant amount of homogeneous plastic flow had occurred in the solder matrix, similar to Fig. 8b, along the entire length of the joint [35].

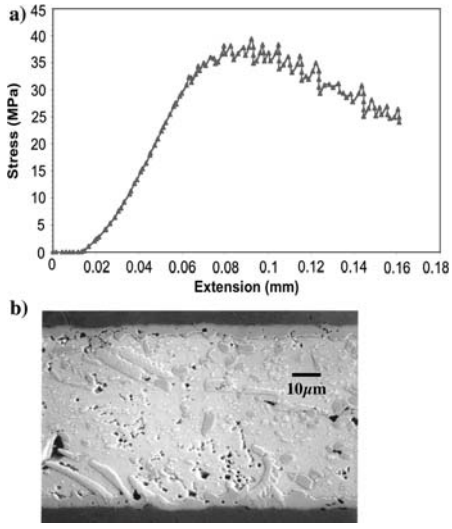

Fig. 8 Shear test (AFPB) results for a solder joint sample made from Sn–3.6Ag–1.0Cu that had been aged for 100 h at 150°C, showing: (**a**) the stress versus strain data, and (**b**) a post-AFPB microstructure of a central region of the joint in cross-section with the Cu substrates on the top and bottom [35]

On the other hand, the weaker example of the Sn–3.6Ag–1.0Cu joints (in Fig. 10a) exhibits a higher yield point than the joint made from Sn–3.7Ag–0.9Cu (see Fig. 9a), but has an immediate drop in load bearing capability, i.e., the maximum shear strength equals the yield strength [35]. This mechanical behavior is consistent with the obvious failure (see Fig. 10d and e) of a long region of the Cu_3Sn/Cu interface, shortly after the crack enters through the ductile matrix on both ends of the joint (see Fig. 10e). The micrograph in Fig. 10d, taken from the middle of the joint, shows no apparent signs of joint matrix flow or intermetallic cracking in addition to the obvious interface debonding at the bottom of the micrograph [35]. This extreme debonding example is actually fairly isolated and ductile failure of the SAC alloy joints is the dominant observation. In other words, localized ductile yielding was observed after aging for 1,000 h in greater than 65% (on average) of solder joint samples made from Sn–3.5Ag and all of the SAC alloys [35]. Figure 11 reveals that although the Sn–3.6Ag–1.0Cu solder joints had the most observations of partial interface debonding (half of the joint samples), the strength level of the joints that failed in a ductile manner was high enough to push it into the strong joint class of the 1,000 h aged samples (see Fig. 7). Figure 11 also indicates that all of the solder joints made from the Co- and Fe-modified SAC alloys exhibited [40] a fully ductile shear failure mode, as will be explained in the following section.

Fig. 9 Summary of the shear test (AFPB) results for a solder joint sample made from Sn–3.7Ag–0.9Cu that had been aged for 100 h at 150°C, showing: (**a**) the stress versus strain data, (**b**) a central region of the joint in cross-section that reveals the localized shear failure mode [35]

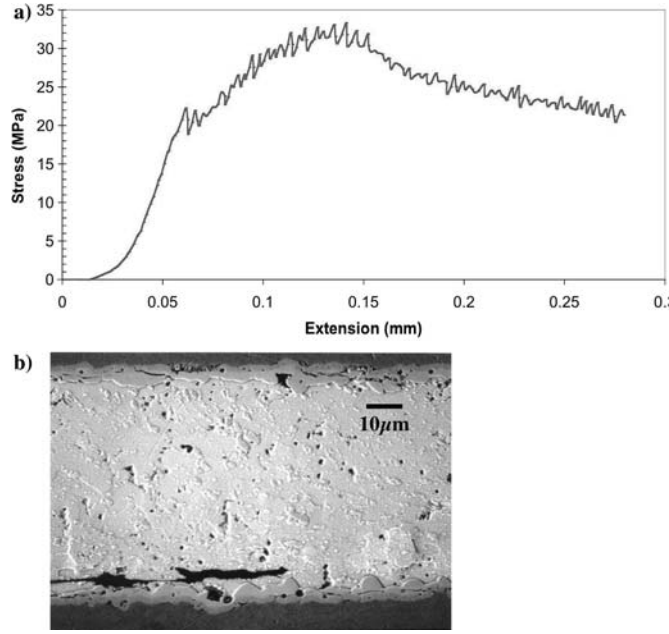

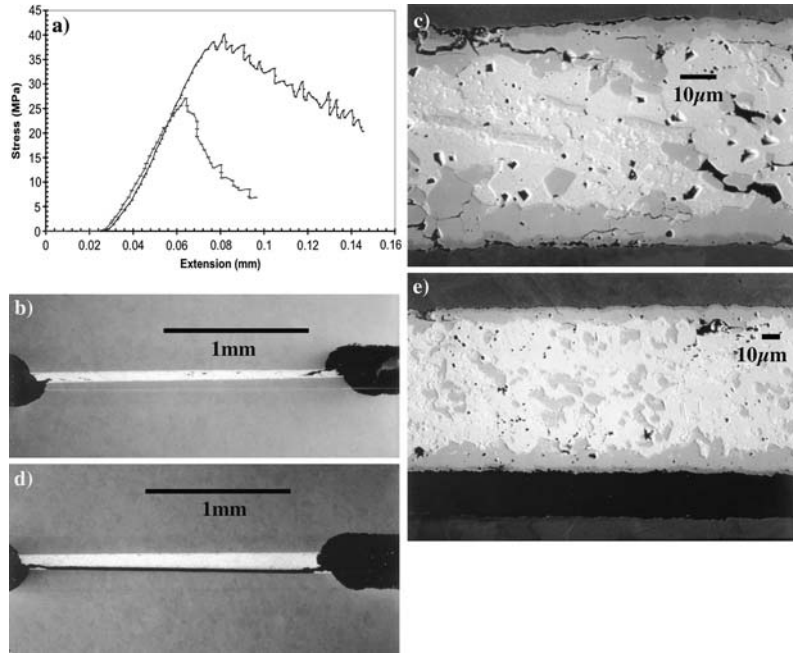

Fig. 10 A summary of the shear failure observations for two solder joints soldered from Sn–3.6Ag–1.0Cu, showing: (**a**) the shear stress versus elongation data for both joints, (**b**) a cross-section SEM micrograph of the strong joint, (**c**) an SEM macrograph of the full width of the strong joint, (**d**) a cross-section SEM micrograph of the weak joint, and (**e**) an SEM macrograph of the full width of the weak joint [35]

Since the first reports of the phenomenon of embrittlement in solder joints made from SAC solder alloys after prolonged high temperature aging in 2003 [56], these thermal aging effects have been the subject of some conflicting reports. Vianco et al. [36] reported on a thorough, well controlled study of Sn–3.9Ag–0.6Cu solder solidified on a Cu substrate, that was subject to thermal aging at several temperatures (70, 100, 135, 170, and 205°C) for a series of prolonged times (1–400 days) to study IMC formation and growth. Earlier studies [36] on thermal aging by the authors had included Sn–3.5Ag and Sn–0.5Ag–4.0Cu solders and pure Sn, also solidified on a Cu substrate. First, the Sn–3.9Ag–0.6Cu solder joint required an aging temperature of at least 135°C to develop a measurable layer of Cu_3Sn between the Cu substrate and the Cu_6Sn_5 IMC layer [36]. However, no void formation at the Cu/Cu_3Sn interface, a precursor observation to embrittlement [35], was detected in these samples even for aging times out to 350 days [36]. The onset of void formation at the Cu/Cu_3Sn interface was observed at 170°C after an aging time in excess of

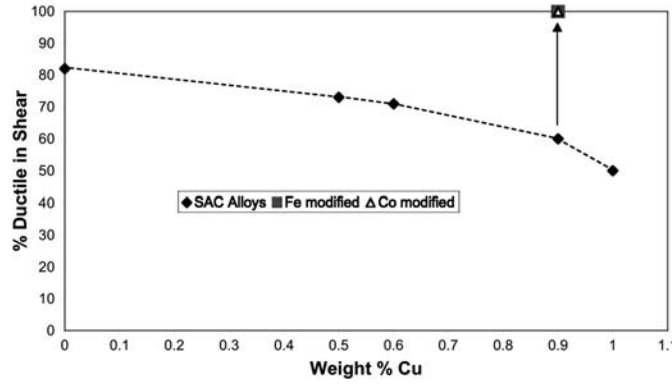

Fig. 11 Summary of the apparent failure mechanisms in the shear test results of the solder joints that were aged for 1,000 h at 150°C, as described in Fig. 7 [40]. Note that the arrow points to the data for the Fe- and Co-modified SAC solder joints

150 days (3,600 h) and was attributed to Kirkendall porosity [57], where longer times and higher aging temperatures promoted void growth and coalescence [36]. Although thermal aging at 150°C was not studied, the results for 170°C would have been expected to exhibit pore formation at a shorter aging time, presumably less than 1,000 h, to be completely consistent with the results in Fig. 11. However, the initial void formation is difficult to detect by microstructural observation alone, since metallographic preparation methods can produce anomalous porosity [35]. Also, shear testing was helpful in detecting the outcome of void formation and, especially, void coalescence, since the shear failure process tends to expose such joint weaknesses [35]. These reasons again may explain why a previous study [36] also failed to detect void formation at the Cu/Cu_3Sn interface in similar samples made from Sn–3.5Ag solder in variance with the results summarized in Fig. 11, which found that 20% of the Sn–3.5Ag joint samples exhibited noticeable embrittlement [35].

For completeness, another study of Sn–Ag–Cu solder joints with Cu also studied embrittlement induced by thermal aging at several temperatures (100, 125, 150, and 175°C) for 3–80 days [20], but did not specify the solder alloy or the reflow conditions of the solder ball samples. Interestingly, this study used a type of high strain rate (drop) tensile loading of components on a board and rapid tensile (pull) and shear testing of individual component (ball) joints to detect the onset of the embrittlement, along with microstructure analysis to observe void development associated with the IMC layers [20]. The authors reported a lack of correlation of the mechanical tests of individual ball joints with the board level failures due to the diversity of loading modes of the joints. However, they did find a consistent association between cross-section microstructure observation of advanced void coalescence at the Cu_3Sn/Cu interface and the percentage of ductile (bulk solder) failure on fracture surface of solder ball pull failures [20]. The void formation was attributed to the Kirkendall effect [57]. The associated data showed that aging conditions of at least 125°C and 20 days (480 h) were needed to promote void coalescence into continuous regions of interface separation and an obvious drop of joint ductility. This thermal aging threshold is lower than even the aging temperature (135°C) for detection of significant Cu_3Sn IMC layer formation by Vianco et al. [36], adding some uncertainty to the results, but the observation of Cu_3Sn/Cu void formation and coalescence is consistent with both the results in Fig. 11 and the microstructure observations of Vianco et al. [36].

2.4 Impact strength of SAC solder joints

In another study of embrittlement of solder joints on thermal aging [17, 18], Sn–9Zn and Sn–8Zn–3Bi solder balls were reflowed three times onto two different substrates, Cu and Au/Ni(P), and subsequently subject to thermal aging at 150°C for up to 1,000 h. While several aspects of this study were significantly different than the other SAC solder studies described above, the use of a well-instrumented (pendulum type) impact tester is an important advance in the quantitative testing of solder joints. The impact specimen was an individual solder ball sample that was joined to a substrate on the bottom only and the miniature ''hammer'' at the end of the pendulum struck the solder ball below the mid-point of the sphere, in a pseudo-Izod type of specimen geometry [17, 18]. Quantitative energy absorption values were obtained for each impact test and the substrate fracture surface of each specimen was analyzed to categorize the fracture mode, i.e., within the bulk (ductile), at the IMC interface (brittle), or mixed, and the results were strongly affected by void formation and IMC layer formation and growth after thermal aging [17, 18]. While the actual results are not important for this report, the use of an instrumented impact tester on an Izod-type specimen to investigate the resistance of a solder joint to impact loading, simulating an accidental dropping incident, is a very worthwhile experimental approach to study this type of reliability problem.

It should be noted that the miniature pendulum-type impact tester discussed above is a custom laboratory instrument [58] and is not broadly available. However, commercial impact test instruments, normally used to test small polymer specimens in an Izod configuration (e.g., Tinius-Olsen model 92-T), are available of a suitable load range to study small solder joint specimens of the type that were used for the asymmetric four point bend (AFPB) shear tests in Fig. 11 [59]. The rectangular specimens (40 mm × 3 mm × 4 mm) were notched only at the solder joint on the leading edge (facing the hammer impact point) and tested at room temperature, although an environmental chamber can be fitted to the instrument to permit testing at sub-ambient and elevated temperatures, similar to a recent Charpy impact study of bulk solder specimens [21]. Some very recent results of such Izod impact testing (see Fig. 12) were published on as-soldered SAC solder and SAC + X joints (based on Sn–3.7Ag–0.9Cu) with Cu [59], but more testing is on-going with thermally aged joint specimens of these SAC joints and some new SAC + X solder joint samples that will be discussed below.

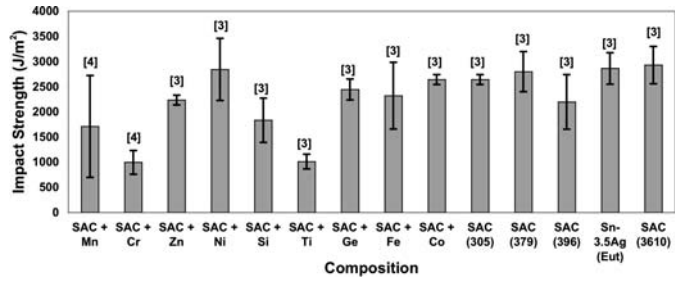

Fig. 12 Summary of the Izod impact strength results from the as-soldered joints in this study, where the standard deviation is superimposed on the bar for each alloy and the number of repeat samples is noted above each bar. The SAC (305) notation, for example, is for Sn–3.0Ag–0.5Cu [59]

2.5 Summary recommendation for SAC solders

In light of the expanding evidence of a reliability issue after extensive aging at high temperatures for solder joints made with SAC alloys, a modified recommendation should be provided beyond the SAC alloy composition, Sn–3.5Ag–0.95Cu, that was provided above. This composition seems preferred based on control of the joint solidification path, i.e., to avoid nucleation of massive Ag_3Sn plates and Sn dendrites and to promote formation of a maximum volume fraction of coupled ternary eutectic microstructure (with an enhanced shear strength) over a range of typical cooling rates. In addition to these highly desirable characteristics for widespread use, some limitations need to be placed on the upper operating temperature of such SAC solder joints. From analysis of all of the accumulated results on thermal aging, it is reasonable to recommend that SAC solder joints (with Cu substrates) of all common compositions should be used for applications with typical operating temperatures less than about 135°C. Actually, it is likely that a higher upper use threshold temperature may be more closely defined between 135°C and 150°C with more study. In fact, it is well known that substrate metallization layers, e.g., Ni or Ni(P) [29] can extend the upper use temperature and it was recently discovered that minor alloying of SAC solders, producing SAC + X solders, also can eliminate the embrittlement problem observed at 150°C out to at least 1,000 h of exposure, as described in the section below.

3 Quaternary Pb-free solder joint microstructures and mechanical properties

In the section above, a thorough review was presented of the use of composition modifications within the Sn–Ag–Cu ternary system to control the solidification path and product phases, especially in solder joints that join Cu substrates. It was also stated that the least desirable solidification product phase seems to be pro-eutectic Ag_3Sn in the form of massive plates or ''blades,'' since it has been identified as a severe limitation on the plastic deformation properties of SAC solder joints [8, 9]. Two basic SAC alloy design strategies to avoid this problem were presented involving either solute-poor (especially low Ag) or slightly hyper-eutectic (Cu-rich) ternary solder alloys. A second problem with SAC solder joints also was identified in the section above that was related to partial embrittlement of joints after extensive high temperature aging. Recognition of this problem lead to the additional recommendation that an upper limit on SAC solder joint temperature exposure be set at approximately 135–150°C, particularly for exposure times on the order of 1,000 h. Therefore, the logic can be seen clearly for the development of a third alloy design strategy involving minor alloy additions to a baseline SAC solder to permit both avoidance of Ag_3Sn pro-eutectic and high reliability use at increased temperatures, perhaps higher than 150°C for times exceeding 1,000 h. This section will present a brief review of the so-called ''SAC + X'' alloy design strategies and the effects of alloy additions on solidification (as-soldered) microstructures and properties, as well as the alloy design efforts targeted at the thermal aging problem.

3.1 Solidification microstructures for SAC + X solders

High undercooling was recognized as a common occurrence and a major influence on the solidification microstructure of Sn–Ag–Cu alloys in bulk melts during early work that explored the existence of a ternary eutectic reaction [4, 7, 29] and in subsequent phase diagram analysis work [6]. At the calculated ternary eutectic composition of Sn–3.7Ag–0.9Cu, the difficulty of nucleation and growth of a coupled ternary eutectic structure has prevented its observation in as-solidified

ingots and solder joints [6]. In fact, the most common as-solidified structure in near-eutectic solder ingots and solder joints (see Fig. 3a–c) is a divorced eutectic microstructure with Sn dendrites as the primary phase and an interdendritic ternary eutectic that freezes subsequently [6]. The high undercooling needed for nucleation of the β-Sn phase in common near-eutectic SAC alloys with reduced Cu (≤0.9Cu) also presents the opportunity for nucleation of Ag_3Sn pro-eutectic plates at a reduced undercooling, producing an undesirable solder joint microstructure, as described above [8].

Thus, one approach to modification of SAC alloys with minor 4th element additions was to minimize the undercooling needed for nucleation of β-Sn phase. As a basis for this recent work, it was noted that low level additions (0.1 wt.%) of some elements, e.g., Zn, Al, Sb, and Bi, had been observed previously to catalyze β-Sn nucleation at significantly reduced undercooling in otherwise pure bulk Sn melts [9, 60]. Of these, SAC + Zn has been pursued aggressively [8] and a Zn addition appeared to promote solidification of coarse Sn dendrites at undercoolings of only 3–4°C in bulk alloy samples, compared to approximately 30°C for the unmodified Sn–3.8Ag–0.7Cu solder alloy. Moreover, when two levels of the Zn addition, 0.1 and 0.7Zn (wt.%), were added to the same SAC solder alloy, the complete elimination of Ag_3Sn plates was achieved for the higher Zn level when the solder was applied to a Cu substrate, even at a cooling rate as slow as 0.02°C/s [8]. Another type of minor 4th element addition, a rare earth (RE) like La or Ce, also seems to catalyze β-Sn (undercooling was not reported), but its primary function [61] was intended to be formation of RE-Sn intermetallic compounds at the Cu interface for improvement of creep properties [61].

Alternatively, some success at nucleation control of a SAC + X solder alloy was achieved by using a Hume-Rothery approach to design a series of possible 4th element additions to a SAC solder alloy, initially Sn–3.6Ag–1.0Cu, that was based on their ability to match closely (<5% mismatch) with the atomic size of Cu [26, 62]. Copper was selected as the object of substitutional alloying because a Cu_6Sn_5 intermetallic compound typically is formed first during SAC solder joint solidification on a Cu substrate, usually as a substrate interface layer. The original intent of the substitutional element in SAC + X was both to modify the as-solidified morphology of the initial Cu_6Sn_5 interfacial layer and to limit growth of the eventual Cu_6Sn_5 + Cu_3Sn interfacial layers under thermal aging conditions [25, 26]. Of the original ''X'' elements tested, two levels of Co (0.15 and 0.45 wt.%) were added to Sn–3.6Ag–1.0Cu and were found to produce an unusual ''coral-like'' intermetallic (apparently Cu_6Sn_5) interface when applied to a Cu substrate, as shown in Fig. 13 [26]. Other X additions to SAC + X solders that produce a similar effect on the intermetallic interface when applied to a Cu substrate include Fe, Ni, and Au [23, 25, 27, 28]. Solder joint solidification with SAC + Co also resulted in formation of massive pro-eutectic Cu_6Sn_5 phases within a complex ternary eutectic matrix. Elemental mapping by electron microprobe indicated that Co was segregated to the tips of some massive pro-eutectic Cu_6Sn_5 phase particles within the solder joint matrix, consistent with a nucleation catalysis effect [22, 26] for Cu_6Sn_5. Subsequently, the undercooling ability of the Sn–3.6Ag–1.0Cu–0.45Co alloy was compared to Sn–3.6Ag–1.0Cu by a fine droplet emulsion technique [26, 63] and was found to decrease undercooling by about 15%, from 142°C to 122°C, confirming the ability of Co to reduce undercooling. It should be noted that much larger undercoolings typically are accessible in solder alloys by the droplet emulsion technique, which may be desirable for increased discrimination of alloy catalyst activity [63].

3.2 Preliminary recommendations for SAC + X solders

Generally, the understanding of minor alloy additions to control nucleation and the solidification pathway of SAC solder alloys is still incomplete, including questions regarding the solidification catalysis mechanism and the minimum required concentration of an active addition. For β-Sn catalysts like Zn, the early formation of Cu–Zn [42] or Cu–Zn- -Sn compounds within the solder melt or at a Cu substrate interface may

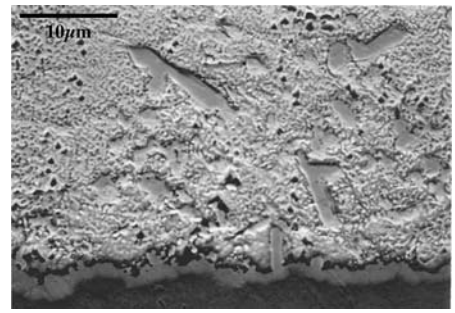

Fig. 13 SEM micrograph, using backscattered electron imaging, showing Cu substrate (bottom), intermetallic Cu/solder interface, and solder matrix microstructures at moderate magnification of joint cooled at 1–3°C/s and made from Sn–3.6Ag–1.0Cu–0.45Co [26]

provide preferred sites for Sn nucleation and dendritic growth. After initial Sn dendrite growth starts, the interdendritic regions are filled with a ternary eutectic microstructure. The addition of Si, Ti, Cr, Mn, Ni, and Ge to a SAC solder also appear to promote the formation of β-Sn in solder joints with Cu [35]. On the other hand, Co appears to catalyze nucleation of Cu_6Sn_5, presumably by the early formation of Co–Sn or Co–Cu–Sn compounds that become a ''seed'' crystal for Cu_6Sn_5 [26]. After the initial Cu_6Sn_5 (pro-eutectic) particles form, the regions between Cu_6Sn_5 particles are filled with a ternary eutectic microstructure. For completeness, it should be noted that the initial work on Co additions was performed with alloys containing a sufficient excess of solute, i.e., Sn–3.6Ag–1.0Cu–0.15Co (at minimum), to promote formation of massive Cu_6Sn_5 phase particles without a catalysis effect. However, more recent work [35] focused on an alloy closely correlated to the calculated ternary eutectic, Sn–3.7Ag–0.6Cu–0.3Co. Without a Co addition the base alloy (Sn–3.7Ag–0.9Cu) joint microstructure exhibits Sn dendrites and interdendritic ternary eutectic, as given in Figs. 3c and 4c. However, the joint microstructure of the near-eutectic SAC + Co solder joint is characterized by small pro-eutectic Cu_6Sn_5 phases and a complex ternary eutectic phase assembly, as given in Fig. 14a and b [39]. Interestingly, the intermetallic interface in Fig. 14a is also very similar to that shown for a solder joint made from a Sn–3.6Ag–1.0Cu–0.45Co solder alloy under equivalent solidification conditions in Fig. 13. These microstructural effects indeed are consistent with the catalytic action of the Co addition, which seems to control the solder joint solidification pathway at this reduced (solute-lean) SAC solder composition. Although such interesting observations have been made, much work remains to determine the limits of both types of catalytic effects and to understand their mechanisms, permitting the maximum benefits for initial solder joint performance and extended reliability. These experiments should include other choices for a fourth element addition (aiming at minimizing the required concentration), extensive calorimetry experiments (to quantify the undercooling effect), and detailed microstructural analysis, including TEM of selected SAC + X solder joints (to probe the nucleant identity and mechanism).

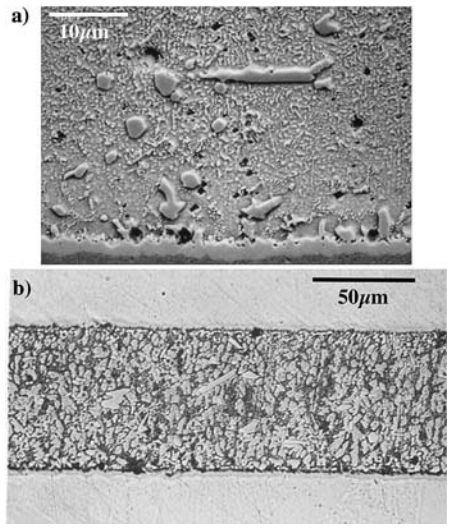

Fig. 14 Microstructure of as-solidified solder joints made from Sn–3.7Ag–0.6Cu–0.3Co, shown as (**a**) SEM micrograph (BEI), and (**b**) optical micrograph [39]

3.3 Thermally aged microstructures and shear strength for SAC + X solders

As thoroughly described in the previous section, mechanical (shear) testing of a series of SAC solder joints and post-test microstructural analysis indicated that after aging at 150°C for 1,000 h, the typical ductile yielding behavior of SAC solder joints was accompanied by observations of a finite probability of some degree of embrittlement in samples made from Sn–3.5Ag and all of the SAC alloys. Microstructural analysis of as-aged (before shear testing) joint samples revealed that Cu_3Sn/Cu interface void coalescence appears to be a precursor condition for the joint embrittlement mechanism. However, the shear test results in Fig. 11 also indicated that all of the solder joints made from the Co- and Fe-modified SAC alloys exhibited a fully ductile shear failure mode. Figure 15 shows an example [35] of the fully ductile shear failure mode for a solder joint of reduced shear strength made with the SAC + Co alloy after aging at 150°C for 1,000 h, which may be compared to the example of SAC joint embrittlement in Fig. 10. This section will summarize the alloy design strategy and beneficial capabilities of these minor alloy additions (and others) to SAC solders for thermal aging resistance.

To probe the mechanism that resulted in resistance to thermal aging embrittlement, initial analysis [35] by line scans with EDS in the SEM indicated that Co and Fe preferentially segregated into the Cu_3Sn and Cu_6Sn_5 intermetallic layers between the solder matrix and the Cu substrate. The preferential segregation was confirmed later by WDS with measurements of increased fidelity [40]. Thus, substitutional alloying of

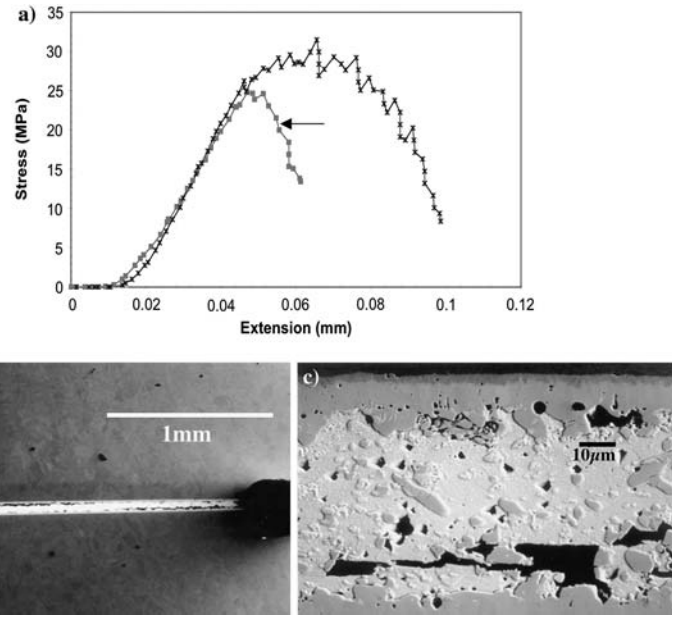

Fig. 15 A summary of the shear failure observations for two typical solder joints made from Sn–3.7Ag–0.6Cu–0.3Co, showing: (**a**) the shear stress versus elongation data for both strong and weak joints, (**b**) a cross-section SEM micrograph of a weak (but ductile) joint, (**c**) an SEM macrograph of the full width (nearly) of the weak joint [35]

Co and Fe for Cu appeared to take place in these intermetallic layers, either during joint solidification or after aging. It should be noted that the apparent substitution of these elemental additions for Cu in the Cu-based intermetallic layers was intended by the alloy design approach, which was based on the Hume-Rothery criteria for extensive solid solubility, i.e., the atomic (metallic) radii mismatch of Fe and Co compared to Cu [24] are – 0.3% and – 1.9%, respectively, i.e., far less than 15% mismatch that is the criteria maximum [62]. More specifically, the alloy design objective was to use the enhanced lattice strain that results from substitutional alloying into the intermetallics to reduce the (vacancy diffusion) rate for interdiffusion of Sn and Cu that is needed for coarsening of the joint microstructure and for void formation and coalescence. The void formation has been presumed to be due to a Kirkendall mechanism [57], where the diffusion flux of Cu is thought to be greater than that of Sn to cause the Cu/Cu_3Sn interface to be the preferred location of the voids [9]. Consistent with this objective, further analysis of the aged microstructures of these joints revealed that both Co and Fe additions reduced the growth rate of the Cu_3Sn layer, although growth of the combined (Cu_3Sn + Cu_6Sn_5) intermetallic layer seemed to be increased, as given in Fig. 16 [35]. Clearly, more study of the diffusion fluxes that cause these apparently contradictory observations is required. However, both of these alloying additions do appear to minimize the formation and coalescence of voids at the Cu_3Sn/Cu interface after thermal aging, preventing the interfacial weakening that is the precursor to joint embrittlement. These initial observations also motivated an extension of the study to look for other additions that can suppress the embrittlement precursor condition and to seek more understanding of the Cu and Sn diffusion flux changes.

In one case, further systematic expansion of the list of possible SAC solder additives that could suppress thermal aging effects utilized a Darken-Gurry ellipse [40] as a further refinement of the Hume-Rothery criteria by adding close electronegativity agreement for predicting considerable substitutional solid solubility for Cu in the Cu_3Sn and Cu_6Sn_5 phases. Thus, a new set of fourth element additions to SAC solder alloys, i.e., SAC + X (X = Si, Ti, Cr, Mn, Ni, Ge, and Zn), were selected on the basis of their predicted ability [40] to substitute for Cu in the intermetallic phase layers that form on a Cu substrate after thermal aging, as a direct extension of the original reason for selection of Co and Fe [24]. A second research effort [64] that sought to address the thermal aging issue in SAC solder joints also identified Ni as a good candidate to add to a SAC solder. However, this effort [64] suggested two criteria; (1) ''relatively large'' solubility in the Cu_3Sn intermetallic phase, as demonstrated by an existing Cu–Sn–X phase diagram, and (2) the ability to increase the liquidus temperature of the Cu_3Sn phase with alloying, requiring

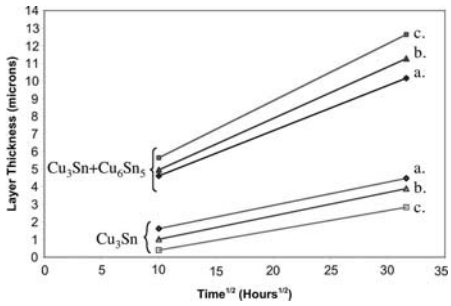

Fig. 16 Comparison of the Cu_3Sn and total (Cu_3Sn + Cu_6Sn_5) intermetallic interface thickness measurements as a function of isothermal aging time at 150°C for solder joints made from Sn–3.7Ag–0.9Cu (**a**), Sn–3.7Ag–0.7Cu–0.2Fe (**b**), and Sn–3.7Ag–0.6Cu–0.3Co (**c**) [35]

also an existing Cu–Sn–X phase diagram. To begin a broader test of the embrittlement suppression hypothesis, the former research effort provided microstructural measurements which indicated that all of the fourth element additions, except Ge, did reduce the measured thickness of the Cu_3Sn layer after aging for 1,000 h at 150°C compared to the base SAC alloy, Sn–3.7Ag–0.9Cu [40]. It should be noted that the previous report did not include data for the growth from thermal aging of the Cu_3Sn layer in SAC + Zn solder joints. A follow-up study [59] reported that these samples actually exhibited no continuous Cu_3Sn layer in the microstructure after 100, 1,000, or 2,000 h of aging at 150°C. The second study [64] also showed microstructural evidence that Ni ''doping'' (<1 wt.%) to a different base SAC alloy, Sn–1.0Ag–0.5Cu, suppressed growth of the Cu_3Sn layer on aging for 120 h at 150°C.

Further investigation by WDS in the former study [40] was conducted of the segregation tendency of X in some SAC + X joints (X = Ni, Mn, and Ge) that had been aged for 1,000 h at 150°C to compare to the segregation behavior in aged joints [35] made from the SAC + Co and SAC + Fe solder alloys. The results of WDS analysis of a SAC + Ni solder joint after extensive thermal aging is shown in Fig. 17 [40]. A later extension of this study also investigated the segregation tendency after thermal aging of Zn in SAC + Zn joints, using the same SAC base composition [59], as given in Fig. 18. As Figs. 17 and 18 demonstrate, both the Ni and Zn additions to the base SAC solder alloy exhibited strong segregation to the Cu/Cu_3Sn interface and into the Cu_3Sn and Cu_6Sn_5 intermetallic layers, similar to the segregation behavior of Co and Fe after the same thermal aging treatment [35]. Figures 17b and 18b also illustrate the difference in the growth behavior of the Cu_3Sn intermetallic phase along the Cu substrate interface after aging for 1,000 h at 150°C. The Cu_3Sn phase grows as an obvious layer in the SAC + Ni case (Fig. 17b), but it grows as a series of disconnected projections from the Cu interface in the SAC + Zn case into the Cu_6Sn_5 phase layer. Also, the follow-up study reported that 2,000 h of aging at 150°C was not enough to promote growth of a continuous layer of Cu_3Sn in the SAC + Zn case [59].

A summary and complete discussion has been given elsewhere [35] of the ambient temperature shear test results for solder joints made with SAC + X solders (X = Fe, Co, Si, Ti, Cr, Mn, Ni, Ge, and Zn), showing the effect of thermal aging, compared to a representative set of SAC solder joints. The average shear strength results generally fall within the range of the data reported in Fig. 7 that includes two of the SAC + X results. Extracted from the SAC + X data, the shear test results for SAC + Ni and SAC + Zn solder joints provided an interesting comparison, where the stress versus elongation curves of joint samples made from the two alloys showed a difference in consistent ductility after the start of plastic deformation. In other words, the SAC + Ni joints had a few samples (one in particular) with less ductility than the rest [40], while the SAC + Zn joints all displayed extended plastic flow at a high stress level [59]. The difference in shear failure behavior between these two cases was illustrated clearly by cross-section micrographs of post-shear test samples, with the least ductile (and weakest) SAC + Ni joint given in Fig. 19 and the least ductile SAC + Zn joint given in Fig. 20 [59]. Obviously, the SAC + Ni joint failed in a fairly brittle manner, while the SAC + Zn joint exhibited fully (localized) ductile shear [59].

Taking the observations in total, some general conclusions may be offered regarding the shear strength behavior and microstructural coarsening and segregation effects after extended isothermal aging at 150°C of solder joint samples (with Cu) made from SAC + X alloys, where X = Co, Fe, Si, Ti, Cr, Mn, Ni, Ge, and Zn. All SAC + X solder joints in the as-soldered, 100 h aged, and 1,000 h aged condition, with the exception of one SAC + Ni sample, experienced shear failure in a ductile manner by either uniform shear of the solder matrix (in the highest strength solders) or by a more localized shear of the solder matrix adjacent to the Cu_6Sn_5 interfacial layer, consistent with many other observations on SAC solder joints [59]. After 1,000 h of aging, some weakening of the Cu_3Sn/Cu interface seemed to occur in only one solder joint made with SAC + Ni that lead to partial debonding during shear testing [59]. Without this isolated observation, only

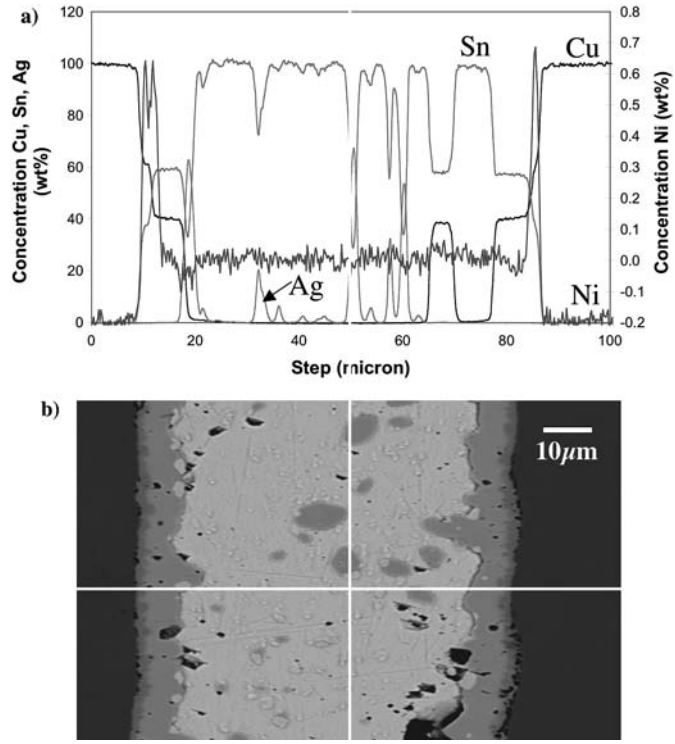

Fig. 17 Typical line scan results for WDS measurements of solder joint made with SAC + Ni alloy that had been aged for 1,000 h at 150°C, showing (**a**) a collection of individual element concentration profiles, and (**b**) an SEM micrograph with a horizontal white line that indicates the transverse path of the elemental scans. Note that the calibration of the Ni composition (right scale on the *y*-axis) has not been adjusted to zero, affecting the absolute values of the concentration [40]

ductile failure was observed in all solder joints made from the SAC + X alloys after aging for 1,000 h. Analysis of aged joint samples by WDS suggests that substitutional alloying of the X addition into the intermetallic layers takes place between the solder matrix and the Cu substrate, with SAC + Ge as the only counter example [35]. This apparent substitutional alloying of the X element for Cu seems to depress the diffusion rate of Cu (most likely) and to minimize the formation and coalescence of voids at the Cu_3Sn/Cu interface, preventing interfacial weakening. Thus, the strategy of modifying a strong (high Cu content) SAC solder alloy with a substitutional alloy addition for Cu seems to be effective for producing a solder joint with Cu that retains both strength and ductility for extremely long periods of isothermal aging (to at least 1,000 h) at high temperatures (to at least 150°C).

3.4 Impact strength of thermally aged SAC + X solder joints

As with the SAC solder joint samples discussed above, the need to add impact testing to the characterization suite of new SAC + X solder alloys has been demonstrated in some recent work [17–19] on the effects of thermal aging on Pb-free solder joints. In other words, to exhibit high reliability a Pb-free solder joint should retain high impact strength and a ductile failure mode after extensive use at high temperatures. As described above, preliminary Izod impact testing was performed [59] on joints samples made from a reduced set of SAC + X alloys with X = Si, Ti, Cr, Mn, Ni, Zn, and Ge and it provided some interesting observations (see Fig. 21). Of these samples, the most impressive were the results after aging for SAC + Ni and SAC + Zn, which maintained impact strength values above 1,500 J/m^2. In fact, the SAC + Zn joints lost only 3% of their as-soldered impact strength after 1,000 h of aging at 150°C. The impact strength retention of aged SAC + Ni joints was not nearly as impressive, with a loss of about 40% of the as-soldered value (see Fig. 21). Broader conclusions will be possible when additional results are available from an increased set of SAC and SAC + X solder alloys.

The Izod sample bar configuration [24] used for the results in Figs. 12 and 21 places the solder joint

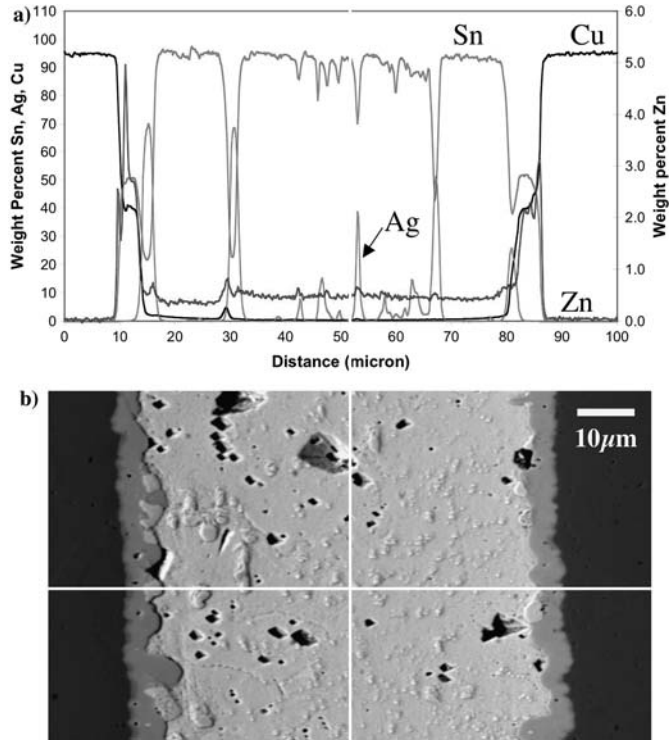

Fig. 18 Typical line scan results for WDS measurements of solder joint made with SAC + Zn alloy that had been aged for 1,000 h at 150°C, showing (**a**) a collection of individual element concentration profiles, and (**b**) an SEM micrograph with a horizontal white line that indicates the transverse path of the elemental scans [59]

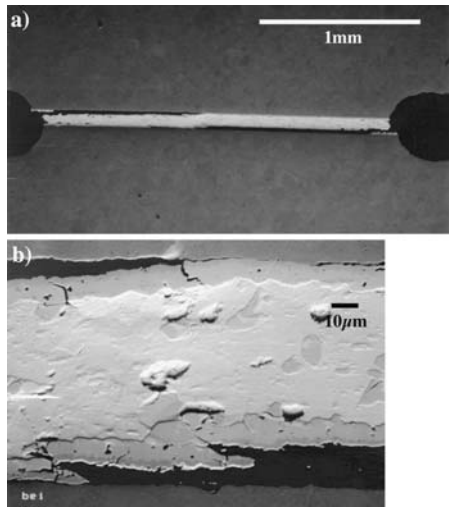

Fig. 19 SEM micrographs of post-AFPB solder joint made with SAC + Ni that displayed reduced ductility, where (**a**) shows the full joint width and (**b**) is a high magnification of the central joint region [59]

line well below the impact point of the pendulum striker, which provides a combined tensile and shear (mixed mode) loading along the joint at an extreme strain rate. A machined notch, aligned on the joint centerline, is also placed on the striker side of the bar, as recommended for the typical Izod impact sample [65] to localize the fracture initiation point. Compared to impact testing of single BGA joints [17, 18], the current Izod sample configuration is more representative of bulk solder joint properties in realistic impact situations and can be practiced on joints that have experienced a wide range of reflow temperatures and cooling rates, simulating either reflow oven practice (as in this study) or the slow cooling of BGA reflow. However, the previous study [17, 18] also accompanied the impact strength measurements with a microstructural assessment of the fracture surface type, i.e., either ductile, brittle, or mixed, which provides a more complete characterization than the current study. Such an assessment is recommended for further Izod impact studies of solder joints.

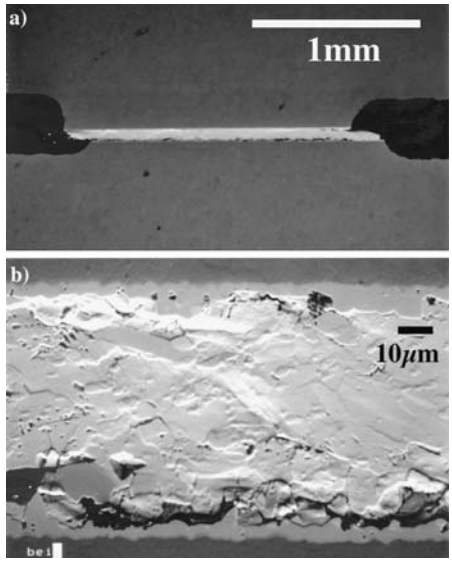

Fig. 20 SEM micrographs of post-AFPB solder joint made with SAC + Zn that displayed minimum ductility, where (**a**) shows the full joint width and (**b**) is a high magnification of the central joint region [59]

3.5 Summary recommendations for SAC + X solders

Although interesting observations have been made on the effects of minor 4th element additions, much work remains to determine the limits of the types of solidification catalyst effects and to understand their mechanisms, permitting the maximum benefits for initial solder joint performance and extended reliability. One goal of this work could be to promote the initial solidification of a high fraction of ternary eutectic microstructure, i.e., minimizing extensive Sn dendritic growth, which may enhance isotropic joint strength and reliability. Of the choices studied, the Co addition and, perhaps, Zn, seem to satisfy this objective. The challenges ahead include discovery of the minimum addition needed to catalyze the desired effect and determination of whether the catalysis effect can persist through multiple reflow cycles. For long-term joint reliability, modifying a strong (high Cu content) SAC solder alloy with a substitutional alloy addition for Cu seems effective for producing a solder joint that retains both strength and ductility after extreme (at least 1,000 h) aging at high temperatures (up to 150°C). Of the choices tested, Co, Fe, and Zn substitutions for Cu seem most attractive from the standpoint of the microstructure (IMC segregation effects and suppression of Cu_3Sn growth and Cu/Cu_3Sn void formation/coalescence) and mechanical properties (retained shear strength and ductility). Although Ni has the same strong interfacial segregation behavior of the others, the discovery of a brittle failure case and the reduced impact strength on thermal aging seem to take it out of prime consideration. Both Fe and Zn have minimal cost, but if reduced amounts of Co prove effective, it may also have an acceptable cost. At this point only anecdotal evidence can be reported of the good (sufficient) solderability (wetting, oxidation, and melting range) of Co, Fe, and Zn, but quantitative studies are needed promptly to facilitate extensive application testing. It is clear that Zn requires a reduced superheat for alloying into a SAC + X solder. Also, Zn retained a remarkable percentage of impact strength after thermal aging, but aged impact results for SAC + Co and SAC + Fe are still in-progress. Confirmation of these preferences by further testing and analysis should be completed to establish the final ranking of the SAC + X choices. Especially if low level additions are proven effective, an expanded testing program that includes SAC + Co, SAC + Fe, and SAC + Zn seems

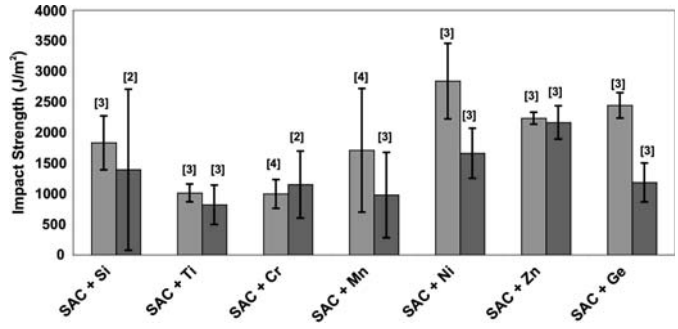

Fig. 21 Comparison of the as-soldered impact strength results with the available results from the 1,000 h aged joints in the study, where the standard deviation is superimposed on the bar for each alloy and the repeat samples are noted above each bar [59]

appropriate to evaluate the performance of these solders in many types of electronic assembly applications, including BGA assemblies.

Acknowledgements Collaborators in this work including Joel Harringa, Bruce Cook, Bob Terpstra, Jack Smith, Tammy Bloomer, Ozer Unal, Chad Miller, and Fred Yost must be recognized for their valuable contributions to these studies. The author is grateful to the Materials Preparation Center of the Ames Laboratory for experimental assistance in solder alloy and wire preparation and in solder joint thermal aging and mechanical testing. Specifically, appreciation is due to Hal Sailsbury for metallographic preparation of the solder joint samples and to Fran Laabs and Alfred Kracher for taking the SEM micrographs and WDS measurements. Bill Wing of the Ames Lab machine shop is also thanked for his careful electrodischarge machining of the joint specimens. Support for the fundamental aspects of this work is gratefully acknowledged from USDOE-BES, Materials Science Division under Contract No. W-7405-Eng-82. Support for other applied aspects of this work is gratefully acknowledged from DOE-EM, under TTP No. CH133001. For recent studies, support is much appreciated from the Iowa State University Research Foundation, under Grant No. 405-25-02. The Advanced Industrial Materials Program of the Office of Industrial Technologies of DOE-EE is also acknowledged for sponsoring a graduate student fellowship during an earlier stage of this study.

References

1. Refer to website at http://www.rohs-news.com/ for information on Restriction on use of certain Hazardous Substances (RoHS) regulations
2. K.N. Tu, A.M. Gusak, M. Li, J. Appl. Phys. **93**(3), 1335–1353 (2003)
3. Refer to websites at http://www.lead-free.org/legislation/, http://www.nemi.org/PbFreepublic/, and http://www.jeida.org.jp/english/information/pbfree/roadmap.html/ for information on relevant organization activities
4. C.M. Miller, I.E. Anderson, J.F. Smith, J. Electron. Mater. **23**, 595 (1994)
5. I.E. Anderson, F.G. Yost, J.F. Smith, C.M. Miller, R.L. Terpstra, U.S. Patent No. 5,527,628, June 18, 1996
6. K.-W. Moon, W.J. Boettinger, U.R. Kattner, F.S. Biancaniello, C.A. Handwerker, J. Electron. Mater. **29**, 1122 (2000)
7. M.E. Loomans, M.E. Fine, Metal. Mater. Trans. A **31A** (4), 1155–1162 (2000)
8. S.K. Kang, D.-Y. Shih, D. Leonard, D.W. Henderson, T. Gosselin, S-I. Cho, J. Yu, W.K. Choi, JOM **56**(6), 34–38 (2004)
9. S.K. Kang, P.A. Lauro, D.-Y. Shih, D.W. Henderson, K.J. Puttlitz, IBM J. Res. Dev. **49**(4/5), 607–620 (2005)
10. D.R. Frear, J.W. Jang, J.K. Lin, C. Zhang, JOM **53**(6), 28–32 (2001)
11. S. Choi, J.G. Lee, K.N. Subramanian, J.P. Lucas, T.R. Bieler, J. Electron. Mater. **31**, 292 (2002)
12. C. Andersson, Z. Lai, J. Liu, H. Jiang, Y. Yu, Mater. Sci. Eng. A **394**, 20–27 (2005)
13. Dr. T. PAN, Ford Motor Company, Dearborn, Michigan, private conversation, February 12, 2001
14. O. Unal, I.E. Anderson, J.L. Harringa, R.L. Terpstra, B.A. Cook, J.C. Foley, J. Electron. Mater. **30**(9), 1206–1213 (2001)
15. W.L. Winterbottom, JOM **45** 20 (1993)
16. F.W. Gayle, G. Becka, J. Badgett, G. Whitten, T.-Y. Pan, A. Grusd, B. Bauer, R. Lathrop, J. Slattery, I.E. Anderson, J. Foley, A. Gickler, D. Napp, J. Mather, C. Olson, JOM **53**(6), 17–21 (2001)
17. M. Date, T. Shoji, M. Fujiyoshi, K. Sato, K.N. Tu, Scripta Mater. **51**, 641–645 (2004)
18. M. Date, K.N. Tu, J. Mater. Res. **19**(10), 2887–2896 (2004)
19. B. Wang, S. Yi, J. Mat. Sci. Lett. **21**, 697–698 (2002)
20. T.-C. Chiu, K. Zeng, R. Stierman, D. Edwards, K. Ano, in *Proceedings of the 54th Electronic Components and Technology Conference* (IEEE, 2004), pp. 1256–1262
21. P. Ratchev, T. Loccufier, B. Vandevelde, B. Verlinden, S. Teliszewski, D. Werkhoven, B. Allaert, in *Proceedings of EMPC 2005, Brugge, Belgium* (IMAPS, 2005)
22. I.E. Anderson, B.A. Cook, J. Harringa, R.L. Terpstra, J.C. Foley, O. Unal, Mater. Trans. **43**, 1827 (2002)
23. J.-Y. Park, R. Kabade, C.-U. Kim, T. Carper, S. Dunford, V. Puligandla, J. Electron. Mater. **32**, 1474 (2003)
24. I.E. Anderson, T.E. Bloomer, J.C. Foley, R.L. Terpstra, in *Proceedings of IPC Works '99 IPC*, Northbrook, IL, paper No. S-03-5 (1999)
25. I.E. Anderson, R.L. Terpstra, U.S. Patent No. 6,231,691 B1, May 15, 2001
26. I.E. Anderson, J.C. Foley, B.A. Cook, J.L. Harringa, R.L. Terpstra, O. Unal, J. Electron. Mater. **30**, 1050 (2001)
27. J.Y. Tsai, Y.C. Hu, C.M. Tsai, C.R. Kao, J. Electron. Mater. **32**, 1203–1208 (2003)
28. C.-M. Chuang, K.-L. Lin, J. Electron. Mater. **32**, 1426–1431 (2003)
29. K. Zeng, K.N. Tu, Mater. Sci. Eng. R **38**, 55–105 (2002)
30. S.K. Kang, D.Y. Shih, K. Fogel, P. Lauro, M.-Y. Yim, G.G. Advocate Jr., M. Griffin, C. Goldsmith, D.W. Henderson, T.A. Sosselin, K.E. King, J.J. Konrad, A. Sarkhel, K.J. Puttlitz, IEEE Trans. Electron. Packag. Manufac. **25**(3), 155–161 (2002)
31. L.C. Shiau, C.E. Ho, C.R. Kao, Solder. Surf. Mount Technol. **14**(3), 25–29 (2002)
32. C.-W. Hwang, K.-S. Kim, K. Suganuma, J. Electron. Mater. **32**, 1249–1256 (2003)
33. K.Y. Lee, M. Li, J. Electron. Mater. **32**, 906–912 (2003)
34. S.K. Kang, R.S. Rai, S. Purushothaman, J. Electron. Mater. **25**, 1113–1120 (1996)
35. I.E. Anderson, J.L. Harringa, J. Electron. Mater. **33**, 1485–1496 (2004)
36. P.T. Vianco, J.A. Rejent, P.F. Hlava, J. Electron. Mater. **33**, 991 (2004)
37. J. Bath, C. Handweker, E. Bradley, "Research update: lead-free solder alternatives," Circuits Assembly (2000), pp. 31–40
38. C.A. Drewien, F.G. Yost, S.J. Sackinger, J. Kern, M.W. Weiser, "Progress Report: High Temperature Solder Alloys for Underhood Applications," Sandia Report, SAND95-0196.UC-704, February 1995
39. I.E. Anderson, B.A. Cook, J. Harringa, R.L. Terpstra, J. Electron. Mater. **31**, 1166 (2002)
40. I.E. Anderson, J.L. Harringa, J. Electron. Mater. **35**(1), 1–13 (2006)
41. R.J. Schaefer, D.J. Lewis, Metal. Mater. Trans. A **36A**, 2775–2783 (2005)
42. S.K. Kang, W.K. Choi, D.-Y. Shih, D.W. Henderson, T. Gosselin, A. Sarkhel, C. Goldsmith, K.J. Puttlitz, JOM **55**(6), 61–65 (2003)
43. M. McCormack, S. Jin, JOM 36–40 (1993)
44. C.M. Liu, C.E. Ho, W.T. Chen, C.R. Kao, J. Electron. Mater. **30**(9), 1152–1156 (2001)

45. A. Garg, I.E. Anderson, J.L. Harringa, A. Kracher, D. Swenson, ''Dissolution of Copper from Substrate Surfaces into Lead-Free Solder Joints,'' poster presentation at 2006 TMS Annual Meeting, San Antonio, Texas (March 2006)
46. D.W. Henderson, T. Gosselin, S.K. Kang, W.K. Choi, D.Y. Shih, C. Goldsmith, K. Puttlitz, U.S. Patent 6,805,974, October 19, 2004
47. I.E. Anderson, K. Kirkland, W. Willenberg, Surf. Mount Technol. **14**(11), 78–81 (2000)
48. W.J. Boettinger, C.E. Johnson, L.A. Bendersky, K.-W. Moon, M.E. Williams, G.R. Stafford, Acta Mater. **53**, 5033–5050 (2005)
49. R.H. Kane, B.C. Giessen, J.J. Grant, Acta Metal. **14**, 605–609 (1966)
50. X. Llovet, G. Galan, Am. Mineral. **88**, 121–130 (2003)
51. S.J.B. Reed, *Electron Microprobe Analysis* (Cambridge University Press, Cambridge, 1993)
52. A.U. Telang, T.R. Bieler, JOM **57**(6), 44–49 (2005)
53. I.E. Anderson, B.A. Cook, J.L. Harringa, R.L. Terpstra, JOM **54**, 26 (2002)
54. S.K. Kang, W.K. Choi, M.J. Yim, D.Y. Shih, J. Electron. Mater. **31**, 1292 (2002)
55. H.-T. Lee, M.-H. Chen, H.-M. Jao, T.-L. Liao, Mat. Eng. A **358**, 134 (2003)
56. I.E. Anderson, B.A. Cook, J.L. Harringa, R.L. Terpstra, in *Proceedings of the International Brazing and Soldering Conference*, ed. by F.M. Hosking (American Welding Society), CD-ROM, 3.7 (2003)
57. R.E. Reed-Hill, in *Physical Metallurgy Principles* (D. Van Nostrand Company, New York, NY, 1973), pp. 386–397
58. T. Morita, R. Kajiwara, K. Yamamoto, K. Sato, M. Date, T. Shoji, I. Ueno, S. Okabe, in *Proceedings of the 16th JIEP Annual Meeting* (JIEP, Tokyo, Japan, 2000), p. 107
59. I.E. Anderson, J.L. Harringa, in *Brazing and Soldering, Proceedings of the 3rd International Brazing and Soldering Conference*, eds. by J.J. Stephens, K.S. Weil (ASM International, Materials Park, Ohio, 2006), pp. 18–25
60. A. Ohno, T. Motegi, Nippon Kinzoku Gakkaishi **37**(7), 777–780 (1973)
61. B. Li, Y. Shi, Y. Lei, F. Guo, Z. Xia, B. Zong, J. Electron. Mater. **34**(3), 217–224 (2005)
62. W. Hume-Rothery, R.E. Smallman, C.W. Haworth, ''The Structure of Metals and Alloys,'' Institute of Metals (1969), p. 124
63. J.H. Perepezko, B.A. Mueller, K. Ohsaka, Undercooled Alloy Phases, eds. by E.W. Collings, C.C. Koch (Metallurgical Society, Inc., Warrendale, PA, 1986), p. 289
64. L. Garner, S. Sane, D. Suh, T. Byrne, A. Dani, T. Martin, M. Mello, M. Patel, R. Williams, Intel Technol. J. **9**(4), 297–308 (2005)
65. ASTM Standard, D-256, ASTM International, West Conshohocken, Pennsylvania, pp. 1–20 (2002)